Electronic supporting information

Nickel-oxido structure of a water-oxidizing catalyst film

Marcel Risch, Katharina Klingan, Jonathan Heidkamp, David Ehrenberg,
Petko Chernev, Ivelina Zaharieva, and Holger Dau

Freie Universität Berlin, FB Physik, Arnimallee 14, 14195 Berlin, Germany

Further experimental detail

Materials

Material	Formula	Purity	Supplier	Head office
Nickel nitrate	$Ni^{II}(OH_2)_6(NO_3)_2$	99 %	ChemPur GmbH	Karlsruhe
Nickel(II) oxide	NiO	99%	Sigma Aldrich Chemie GmbH	Munich
Nickel(III) oxide	Ni_2O_3	unknown	Chemos GmbH	Regenstauf
Boric acid	H_3BO_3	p.A.	Merck KGaA	Darmstadt
Potassium hydroxide	KOH	> 86 %	Sigma Aldrich Chemie GmbH	Munich
ITO on PET, 60 Ω/sq	n/a	n/a	Sigma Aldrich Chemie GmbH	Munich
Potassium phosphate	KH_2PO_4	99.5 %	AppliChem GmbH	Darmstadt
Potassium phosphate, dibasic	K_2HPO_4	99.5 %	AppliChem GmbH	Darmstadt
Cobalt nitrate	$Co^{II}(OH_2)_6(NO_3)_2$	99.9 %	Sigma Aldrich Chemie GmbH	Munich
Lithium cobalt dioxide	$LiCoO_2$	99.8 %	Sigma Aldrich Chemie GmbH	Munich

All solutions were prepared from purified, deionized water (Millipore milliQ water, >18 MΩ·cm).

A solution of inorganic potassium phosphate, KP_i, was prepared as a mixture of ~40% KH_2PO_4 and ~60% K_2HPO_4 at a total P_i concentration of 0.1 M. We verified that the pH of the resulting electrolyte was 7.0; if necessary a fine adjustment of the pH was achieved by addition of small aliquots of 1 M KH_2PO_4 or 1 M K_2HPO_4. For deposition, we added $Co^{II}(OH_2)_6(NO_3)_2$ solution, so that the final concentration in the electrolyte solution was 0.5 mM. Filtration was not necessary and the solution remained clear for the duration of the deposition.

Inorganic borate, B_i, was prepared from H_3BO_3, with a resulting concentration of 0.1 M. The pH of the electrolyte was adjusted to 9.2 using saturated KOH solution. $Ni(OH_2)_6(NO_3)_2$ was added to yield a final concentration of 1.0 mM, subsequently stirred for several minutes, then filtrated through a cellulose folded filter (Rotilabo, Typ 600P, 150 mm). The filtrated solution remained clear and free from further precipitates during the NiCat growth.

Electrochemistry

All potentials are given relative to the potential of the normal hydrogen electrode (NHE). We employed a single compartment, three electrode setup driven by an SP-200 potentiostat (Bio-Logic SAS, Claix). Corrections for the resistance of working electrode and electrolyte solution were not applied during deposition. The working electrode was indium tin oxide (ITO) coated polyethylene terephthalate (PET) purchased from Sigma-Aldrich (60 Ohm/sq.); the counter electrode was a 25 x 25 mm² platinum grid (100 mesh, 99.9 %, Sigma Aldrich GmbH), and a mercury sulfate reference electrode (650 mV *vs.* NHE) was used.

XAS sample preparation

The NiCat-films were formed by electrodeposition on indium tin oxide (ITO) coated PET sheets (Sigma-Aldrich, 60 Ohm/sq.) with dimensions of 1 x 2.5 cm², which we cut from a larger sheet. Polyethylene terephthalate (PET) is nearly transparent for hard X-rays, *i.e.* the transmission is > 90 % for a 130 µm PET sheet within the energy rage of our XAS experiments. Good electrical contact with the conducting ITO layer was assured by adding a small strip of conducting copper tape (Farnell GmbH). For each electrode, the conductivity of this interface was tested using a digital laboratory multimeter. The copper tape on the electrode was connected to the potentiostat with an alligator clip. We checked that neither the copper tape nor the clip made contact with the electrolyte at any time.

The electrolytes were aqueous solutions of 1 mM $Ni(OH_2)_6(NO_3)_2$ in either 0.1 M B_i, pH 9.2, or 0.1 M KP_i, pH 7; preparation details of the solutions are described above. Potentiostatic catalyst formation was carried out at 1.30 V in B_i or 1.57 V in case of KP_i (potentials not corrected for iR drop). The resulting NiCat samples on the PET support were carefully rinsed with the Ni-free KP_i or B_i solution, depending on which solution was present during deposition. Then, the samples were conditioned at the same potential as used during deposition (1.30 V in B_i, 1.57 V in KP_i) for 2 min in the Ni-free electrolyte. Finally, the samples were quickly blow-dried using dry air. A single layer of Kapton tape (50 µm, Goodfellow GmbH) was used to fix the sample on its mount. This mount is a custom-made, 1 mm thick polyvinyl chloride (PVC) sheet which has a 1.1 x 1.5 cm² window, through which the NiCat film was accessible in XAS measurements. The NiCat/ITO/PET electrode was fixed on the mount with the Kapton tape such that there was no Kapton tape in the path of the X-ray beam. Also the copper tape was not directly exposed to the X-ray beam because the beam was blocked by the PVC of the mount. Finally, the mounted NiCat was frozen in liquid nitrogen within 1 min after conclusion of the conditioning step. The samples were stored in liquid nitrogen for no longer than two weeks before the synchrotron measurement.

The samples of the NiO and Ni_2O_3 powder references were prepared by mixing the commercially available powders with boron nitrate (BN) in volume ratio 1:3 (oxide:BN). The powders were carefully ground for 10-15 min using mortar and pestle made from agate stone. The sample compartment for powder measurements was

covered on both sides with Kapton tape (50 µm thick, Goodfellow GmbH) after filling with the sample powder. Each powder sample was enclosed in a cavity (PVC frame and two Kapton windows), which was 1 mm thick, 1.5 mm wide, and 1.1 mm high. These samples were stored in liquid nitrogen until use in the XAS experiment.

XAS setup and data evaluation

The XAS measurements at the Ni K-edge were performed at the KMC-1 bending-magnet beamline of the Helmholtz-Zentrum Berlin for Materials and Energy (formerly BESSY II, Berlin). The beamline optics and beam characteristics are discussed elsewhere [1]. The excitation energy (scan range 8150-9400 eV) was selected by a double-crystal monochromator (Si-111). A feedback system was used to maximize the flux while scanning the energy (dynamic detuning to the top of the rocking curve). We did not detect any indications that higher harmonics of the excitation energy passed the monochromator.

The sample was kept in a cryostat (Oxford-Danfysik) for which we custom-built an optimized housing. The sample was kept at 20 K during measurements using a liquid-helium flow system. The sample compartment contained a 200 mbar He atmosphere. In the volume between sample compartment and the outer cryostat housing, a vacuum of typically 2-3 x 10^{-5} mbar was maintained. The XAS samples consisting of the ITO electrodes covered with either the CoCat or the NiCat were mounted such that the angle between the NiCat surface and the incident beam was 45°. The fluorescence detector was installed perpendicular to the X-ray beam. In order to minimize the radiation damage to the investigated samples, the cryostat was installed about 3 m away from the focal point of the beamline optics, thereby decreasing the X-ray intensity (per area) by increasing the spot size. At the out-of-focus position, the area irradiated by the X-rays was about 1 mm x 0.5 mm. A filter foil (10 µm Co, 99.9 %, Goodfellow GmbH) was put directly in the sample compartment between the NiCat surface and the window facing the fluorescence detector.

We used a fluorescence detector with 13 Ge elements (Ultra-LEGe detectors, Canberra GmbH). The energy resolution was tested with a ^{55}Fe source (5.9 keV) and is approximately 150 eV for the shaping time of 2.5 µs that we use for EXAFS experiments of transition metal *K*-edges. The 13 detector elements are protected by a thin aluminum polymer cap, which also serves as a heat shielding. The nominal active area is 50 mm² per element. The detector was operated at 500 V and the signals were amplified by integrated pre-amplifiers (type, 3102 D). The signal processing was done using analog components, namely 13 shaping amplifiers of type 2026 and 13 single channel analyzers of type 2030. The energy window was set to the K_α-emission of Ni.

Each spot on the NiCat sample was exposed for about 35 min to synchrotron radiation. We changed the spot on the sample by 0.5 mm (vertically) after each scan. The spectra of the 13 channels were averaged for each spot on the samples. The average total fluorescence counts of the edge jump (definition in following paragraph) per spot in the energy window were 23400 for the NiCat deposited with KP_i and 41600 for the NiCat deposited with B_i.

For the KP_i-NiCat, we evaluated data from two spots on the same sample. Six spots on two separate sample preparations were evaluated for the B_i-NiCat. In the collected spectra, we found no significant differences between spots detected on the same sample and spots detected on a second sample prepared by the same protocol.

The primary data evaluation involved several steps. After dead-time correction, the fluorescence spectra were normalized by the signal of an ionization chamber placed before the cryostat. The energy axis of the data was calibrated as described below. Then, the signal-to-noise ratio was estimated by fitting a straight line to the data points at the end of the EXAFS region (9250-9400 eV), where EXAFS oscillations are negligibly small; and the root of the squared differences between line and data points was calculated (rms noise). The magnitude of the edge jump was approximated by the difference between the average of 5 points near the pre-edge and the average of 5 points near the end of the scan range. Spectra from different spots were then averaged with weights given by the edge-jump magnitude divided by the rms noise. Subsequently, we subtracted the background of the pre-edge region, which was well described as a constant offset, from the fluorescence spectra. The spectra were divided by a 2^{nd} order polynomial in order to normalize the edge jump to 1.0 for the XANES analysis. For EXAFS analysis, the data was not divided by a polynomial but a spline function was employed (see below).

The EXAFS oscillations were extracted by minimizing a "knot-spline" with 5 knots between 8335 and 9365 eV, which then was subtracted from the data. The energy axis was shifted by subtraction of 8335 eV (E_0) and transferred into the *k*-domain (wavevector space) [2]. Then, the number of data points was reduced by appropriate averaging to yield a constant step size of approximately 0.075 $Å^{-1}$ (~210 data points between 1 and 16 $Å^{-1}$).

During each scan, the fluorescence data and the spectra of an energy reference were recorded simultaneously. After passing the sample in the cryostat, the X-ray beam passed an ionization chamber placed immediately after the cryostat (I_1), a chamber containing the reference material, and another ionization chamber (I_2).The negative natural logarithm of the I_2-signal was calculated for obtaining a relative measure of the absorption (The signal of I_1 was featureless and noisy. Thus, normalization by I_1 was found to result in a significant decrease of the signal quality and was not applied). The thereby obtained absorption signal was smoothed and then the derivative was calculated analytically from the coefficients of a polynomial spline. We checked carefully that no features of the original dataset were lost or smeared out in the smoothing processes. For energy calibration, we shifted the energy axis of the experimental data by an offset such that the first maximum in the derivative of the reference signal aligned with the value of 8333 eV reported by Bearden and Burr[3].

The powderous Ni reference samples were measured in absorption mode (two scans on different spots for each sample). The absorption signal was calculated by taking the negative natural logarithm of the signal in the I_1 ionization chamber after division by the signal of the I_0 ionization chamber placed in the path of the X-ray beam before the cryostat. A linear background was determined in the pre-edge region and subtracted. Then the

spectrum was divided by a 3rd order polynomial previously fit to the data in the EXAFS region, in order to normalize the edge jump to unity. The $LiCoO_2$ and CoCat spectra were identical to those discussed in reference [4] and [5], respectively.

EXAFS simulations

All simulations were performed using the in-house software packages SimX [6] or SimX lite. The EXAFS data was extracted as described above, then weighted by k^3 and simulated (least-squares fit) in *k*-space (without any type of Fourier filtering).

An EXAFS spectrum, $\chi(k)$, is given by the sum of the contributions of n_{shell} atomic shells (that is, groups of elements with the same atomic number and similar distances from the X-ray absorbing atom, *e.g,* the six oxygen atoms that surround the X-ray absorbing Ni ion in a Ni octahedron). For EXAFS simulations, the spectrum is described by the following equation [2, 7]:

$$\chi(k) = S_0^2 \cdot \sum_i^{n_{shell}} A(R_i,k)_i \cdot N_i \cdot \exp\left(-2\sigma_i{}^2 \cdot k^2\right) \cdot \sin(2k \cdot R_i + \phi_i), \qquad \text{Eq. (S1)}$$

where S_0^2 is the amplitude reduction factor, $A(R,k)_i$ represents the scattering amplitude and ϕ is the phase correction (both were obtained from *ab-initio* Feff calculations), N_i is the number of neighbors in the i^{th} atomic shell, σ_i is the Debye-Waller parameter of the i^{th} atomic shell, and R_i is the distance between the X-ray absorbing atom (absorber; *e.g.* Ni) and the atoms in the i^{th} atomic shell (backscatterer).

The phase functions ($A(R,k)$, ϕ) were obtained using Feff 9.05 [8-9]. For the simulation at the Co *K*-edge, the coordinates were obtained from a fragment of the $LiCoO_2$ structure (CoO_2 layer) with 10 cobalt atoms and 32 oxygen atoms, see Fig. 8 in reference [10]. The scattering paths were obtained up to a radius of 6 Å for up to "four-legged" paths. The simulation results with the new phase functions for Co did not deviate significantly from those reported previously [5]. However, the energy shift of E_0 (relative to the value used for extraction of the experimental EXAFS data) was increased to 3.5 eV (found by EXAFS simulations of the experimental data). For the simulations at the Ni *K*-edge, identical parameters were used in Feff and the coordinates were taken from the same cluster with Ni substituted for Co (*i.e.* a Ni oxide layer with 10 Ni and 32 O atoms). The energy shift of the Ni phase functions was 7.0 eV.

The following function describing the simulation error was minimized:

$$\varepsilon(\boldsymbol{a}) = \sum_i^n (\chi(k,\boldsymbol{a})_i - y_i)^2, \qquad \text{Eq. (S2)}$$

where $\boldsymbol{a}$ denotes a vector containing all fit parameters, $\chi(k,\boldsymbol{a})$ is the EXAFS model function as defined by

Eq. S1, and y_i corresponds to the *unfiltered* experimental data (n data points). For minimization, a Levenberg-Marquardt algorithm was used. In the following, the minimum of $\varepsilon(\boldsymbol{a})$ is called ε_m. A set of parameters, $\boldsymbol{a}_{min}$, is defined such that $\varepsilon(\boldsymbol{a}_{min}) = \varepsilon_m$.

Parameter error estimation

The parameter errors were calculated *after* the parameters had been optimized using the method discussed in the following.

First, the data was Fourier-isolated according to the following protocol: (1) Fourier transform from k-space to R-space for data corresponding to the k-range of 1.6 Å^{-1} to 16.2 Å^{-1}, without using a window function; (2) back transformation from R-space to k-space (elsewhere also called q-space [11]) for data corresponding to the R range from 0.0 Å to 8.1 Å. Subsequently, the sum in Eq. S2 was calculated for the Fourier-isolated EXAFS spectra to obtain a new minimum denoted ε_m^*. We confirmed that the optimized parameters $\boldsymbol{a}_{\mathbf{min}}$ were the same for the filtered and the unfiltered dataset.

The degree of freedom of EXAFS simulations, ν, is defined as follows:

$$\nu = N_{ind} - \dim(\boldsymbol{a}), \qquad \text{Eq. (S3)}$$

where $\dim(\boldsymbol{a})$ denotes the number of independent simulation parameters, which was 7, 10 or 12 in our simulations (see Table S2). The number of independent data points is estimated according to $N_{ind} \approx 2\,\Delta k\,\Delta R / \pi$ [12], where the simulation range corresponds to Δk (either 9 or 12 Å^{-1}, see Table S2). The four simulated peaks in the FT correspond to a ΔR-value of 5.0 Å. In our simulations, typical degrees of freedom were between 20 and 30.

We assume that ε_m^*/ν provides an estimate of the statistically relevant (averaged) experimental error, which we use to normalize the simulation error, $\varepsilon(\mathbf{a})^*$. The error $\varepsilon(\mathbf{a})^*$ is calculated by Eq. S2 for the data obtained by the Fourier-isolation procedure described above. Thus:

$$\varepsilon^{norm}(\boldsymbol{a}) = \nu \frac{\varepsilon(\boldsymbol{a})^*}{\varepsilon_m^*}. \qquad \text{Eq. (S4)}$$

Moreover we assume a normal distribution of the individual errors and a chi-square distribution of the squared errors. Now, for each fit parameter (a_i) holds that its respective 1σ error range (68% confidence interval) corresponds to an increase in the normalized error sum by one [13]:

$$\varepsilon_\sigma^{norm}(\boldsymbol{a}) = \nu + 1. \qquad \text{Eq. (S5)}$$

On these grounds, we obtained the parameter variances from the diagonal of the covariance matrix (*i.e.* the inverse Hesse matrix ($d^2\varepsilon^{norm}(\boldsymbol{a})/d\boldsymbol{a}^2$, calculated at $\boldsymbol{a}_{\mathbf{min}}$) [13]. The 1σ error range of parameter a_j is then obtained by taking the square root of the diagonal elements, c_{jj}, in the covariance matrix.

Measure of the fit quality

We defined a measure of the fit error which quantifies the deviations between experimental and simulated spectra relative to the overall magnitude of the experimental spectrum.

$$R_f = \frac{\sum_i^n |\chi(k,\boldsymbol{a})_i^* - y_i^*|}{\sum_i^n |y_i^*|}. \qquad \text{Eq. (S6)}$$

In Eq. S6, an asterisk denotes the operation of Fourier isolation (as described further above) for the *R*-range of interest (herein from 1 Å to 6 Å). The value of this Fourier-filtered *R*-factor usually is presented as a percent figure. The R_f-value provides a useful measure of the fit quality; an R_f exceeding 25 % typically indicates a clearly insufficient quality of the fit. (We note that the R_f-value differs from the 'goodness of fit' occasionally used in EXAFS analyses. The number of the independent data points and the number of the fit parameters does not affect directly the R_f-value calculated by means of Eq. S6.)

Electrochemical experiments (Fig. S1)

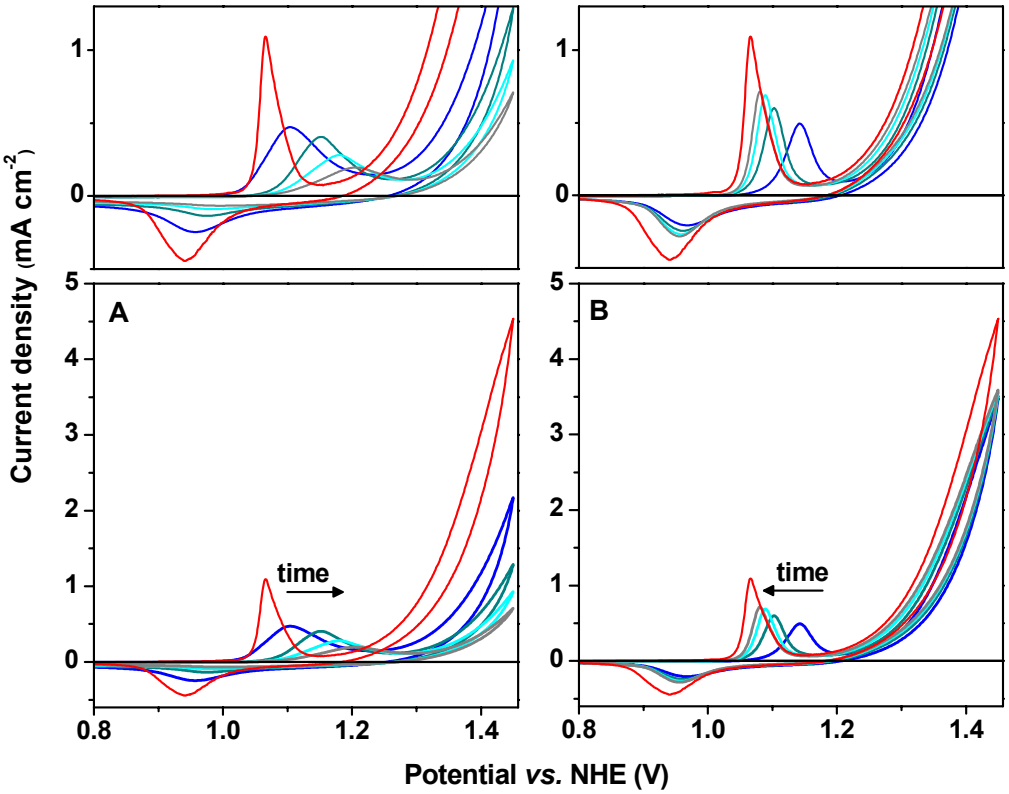

Figure S1. Cyclic voltammograms (CV) for an exchange of the anion (borate, phosphate) after electrodeposition of the NiCat.
(A) NiCat electrodeposited in B_i (1.15 V, 3 mC/cm^2, pH 9.2) and measured in KP_i at pH 9.2.
(B) NiCat electrodeposited in KP_i (1.28 V, 3 mC/cm^2, pH 9.2) and measured in B_i at pH 9.2.
We compensated for the iR drop during both deposition and the CV experiments. After formation of the NiCat, the buffer was exchanged and a series of CVs was recorded (scan rate: 20 mV/s, duration of each cycle: 75 s). The 1st to 4th cycles are shown. The CVs were smoothed over a range of 10 mV. In all panels, the red trace shows the cyclic voltammogram of a NiCat electrodeposited in B_i (1.15 V, 3 mC/cm^2, pH 9.2) and measured in B_i at pH 9.2. In the top panels, the presentation of the graphs is such that the changes in the pre-wave (before onset of the catalytic wave) are better visible.
The shown CVs suggest an exchange of B_i and P_i for NiCat films deposited in one electrolyte and operated in another electrolyte. The performance decreases for operation in KP_i at pH 9.2, whereas it increases for operation in B_i at pH 9.2. Further investigations are required to characterize and understand the anion exchange more completely.
The red trace demonstrates the high catalytic activity for oxygen evolution of the NiCat since the Faradic efficiency is close to 100 %.

Extended XANES spectra and edge positions (Fig. S2, Table S1)

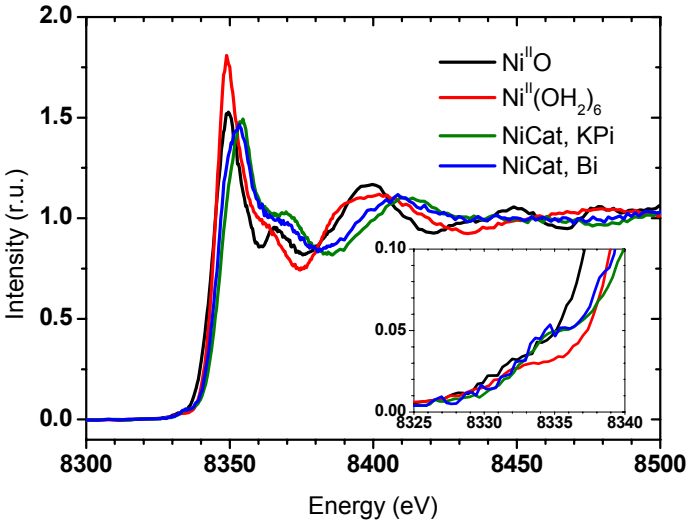

Figure S2. Extended range of the XANES spectra shown in Fig. 1. The spectrum of a Ni hexaqua sample is shown in addition. The inset magnifies the pre-edge region.

Table S1. Selected edge positions of reference compounds, the edge positions of the NiCat in Figs. 1 and S2 as well as comparison to literature values.

Compound	Half-height (eV)	Integral (eV)	Reference
NiCat, B_i	8345.0	8345.3	This work
NiCat, KP_i	8343.9	8344.2	This work
"$Ni^{III}_2O_3$" [a]	8342.2	8343.0	This work
$Ni^{II}(OH_2)_6$	8342.9	8343.0	This work
$Ni^{II}O$	8341.9	8342.3	This work
$Ni^{II}(OH)_2$	8341.7[b]	n/a	[14]
$Ni^{II}O$	8341.9[b]	n/a	[14]
$KNi^{IV}IO_6$	8345.8[b]	n/a	[14]
$LaNi^{III}O_3$	0.0[c]	n/a	[15]
$La_2Ni^{II}O_4$	-2.0[c]	n/a	[15]
$LaNi^{I}O_2$	-4.4[c]	n/a	[15]

The integral method [16-17] was used with limits of $0.15<\mu<1.0$.

[a] Reference was not completely in oxidation state 3+.

[b] The energy calibration in reference [14] was different from ours. To make the positions comparable to our data, we have shifted all edge positions reported in [14] by a constant offset such that the edges of the NiO samples are aligned.

[c] The XANES spectra were normalized to the magnitude of the white line. Therefore, the half-height edge positions reported by Crespin *et al.* [15] are not directly comparable to those normalized by the edge jump (as done for the other values presented in this table).

EXAFS oscillations in *k*-space (Fig. S3)

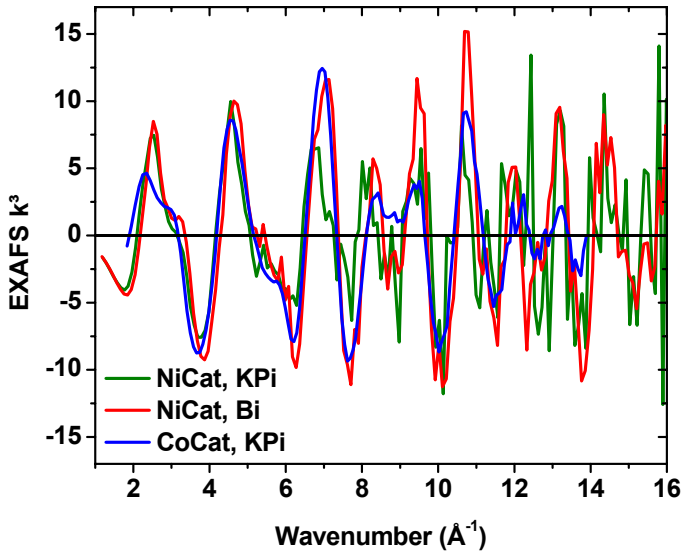

Figure S3. EXAFS data of the NiCat and the CoCat. The simulation range used for the fit results presented in Table S2 extends up to 12 A^{-1} or up to 15.0 A^{-1}.

Additional EXAFS simulation results (Table S2, Fig. S4)

Table S2a. EXAFS simulation results at the Co K-edge for the $LiCoO_2$ reference and the CoCat.

Simulation	Interaction	N	R (Å)	σ (Å)	Rf
1: $LiCoO_2$[a]	Co-O	5.9	1.91	0.046	12.8 %
35-850 eV	Co-Co	6.2	2.81	0.041	
3.0-15.0 $Å^{-1}$	Co-Co	7.0	4.93	0.046	
$S_0^2 = 0.6$	Co-Co	5.8	5.61	0.033	
2: $LiCoO_2$[a]	Co-O	5.9	1.91	0.046	13.1 %
35-850 eV	Co-Co	6.2	2.81	0.041	
3.0-15.0 $Å^{-1}$	Co-Co	6.0[b]	4.93	0.039	
$S_0^2 = 0.6$	Co-Co	5.7	5.61	0.032	
3: $LiCoO_2$[a]	Co-O	5.9	1.91	0.046[c]	12.8 %
35-550 eV	Co-Co	6.3	2.81	0.041[c]	
3.0-12.0 $Å^{-1}$	Co-Co	6.0[d]	4.94	0.039[c]	
$S_0^2 = 0.6$	Co-Co	5.6	5.60	0.032[c]	
4: CoCat[d]	Co-O	5.6	1.89	0.046[c]	17.1 %
35-550 eV	Co-Co	2.5	2.81	0.041[c]	
3.0-12.0 $Å^{-1}$	Co-Co	0.4	4.83	0.039[c]	
$S_0^2 = 0.7$	Co-Co	0.3	5.62	0.032[c]	
5: CoCat[d]	Co-O	6.1	1.89	0.054	12.2 %
35-550 eV	Co-Co	4.4	2.81	0.071	
3.0-12.0 $Å^{-1}$	Co-Co	0.3	4.80	0.039[c]	
$S_0^2 = 0.7$	Co-Co	0.4	5.62	0.032[c]	

Explanation of symbols below Table S2b.

Table S2b. EXAFS simulation results at the Ni K-edge and Mn K-edge, that is of the NiCat and of a Mn-Ca catalyst for reference.

Simulation	Interaction	N	R (Å)	σ (Å)	Rf
6: NiCat (B_i)	Ni-O	5.7	1.88	0.046[c]	11.6 %
35-550 eV	Ni-Ni	4.5	2.81	0.041[c]	
3.0-12.0 $Å^{-1}$	Ni-Ni	2.3	4.86	0.039[c]	
$S_0^2 = 0.6$	Ni-Ni	1.8	5.60	0.032[c]	
7: NiCat (B_i)	Ni-O	5.7	1.88	0.046[c]	13.8 %
35-850 eV	Ni-Ni	4.4	2.81	0.041[c]	
3.0-15.0 $Å^{-1}$	Ni-Ni	2.3	4.89	0.039[c]	
$S_0^2 = 0.6$	Ni-Ni	1.6	5.59	0.032[c]	
8: NiCat (B_i)[d]	Ni-O	6.3	1.88	0.055	13.5 %
35-850 eV	Ni-Ni	4.4	2.81	0.041	
3.0-15.0 $Å^{-1}$	Ni-Ni	2.3	4.89	0.039[c]	
$S_0^2 = 0.6$	Ni-Ni	1.6	5.59	0.032[c]	
Mn Catalyst **1**[f]	Mn-O	5.5 / 0.5	1.90 / 2.34	0.063	n/a
20-1000 eV	Mn-Mn	2.7	2.86	0.063[b]	
2.3-16.2 $Å^{-1}$	Mn-Mn	0.8	4.99	0.063[b]	
$S_0^2 = 0.7$	Mn-Mn	2.0	5.52	0.063[b]	

[a] The spectrum was taken from reference [4]. The EXAFS analysis was performed again herein.

[b] Value was fixed in simulation.

[c] These σ-values were taken from the simulation of $LiCoO_2$ (simulation ***2***).

[d] The spectrum was taken from reference [5]. The EXAFS analysis was performed again herein.

[e] Simulation ***8*** is also shown in Table 1 of the main text.

[f] The EXAFS analysis was reproduced from reference [18] .

The R_f value was calculated between 1 and 6 Å (reduced scale) and provides a measure of the fit quality in percent. The FT for the R_f calculation was computed between 12 and 735 eV with a $\cos^2$ function as the window function covering the entire FT range.

Only single-scattering paths were used to simulate the interactions with atomic distances below 5 Å. For the M-M interaction near 5.6 Å, we used the two multiple scattering paths with the highest amplitude in *k*-space: (1) the 4-legged scattering path with the absorber at an end point of the linear 'chain' of three atoms (4 legs with 2.8 Å in either direction); and (2) the 3-legged paths with the absorber at an end point of the linear chain (two legs with 2.8 Å in one direction and a leg of 5.6 Å length in the other direction.

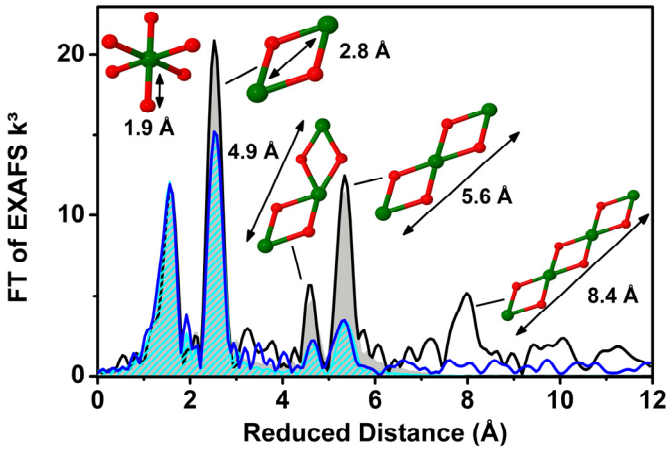

Figure S4. Fourier transforms (FT) of the EXAFS spectra of $LiCoO_2$ (black, simulation ***2***) and of the NiCat (blue, simulation ***8***) in Table S2. The simulated EXAFS spectra are indicated by areas. The FT was calculated between 10 and 1000 eV with a $\cos^2$ window covering the first and last 10% of the FT range (data unaffected by the FT window in 80% of the range).

Literature survey, Ni-O bond lengths (Table S3)

Table S3. Ni-O bond length for Ni^{II}, Ni^{III}, $Ni^{III,IV}$ and Ni^{IV} oxides from XRD and EXAFS experiments. For each oxidation state, we calculated the arithmetic mean. The errors were obtained from the experimental scatter (95 % confidence interval; normalized by the square root of the sample number). The label 'calibration curve' denotes the value obtained from the formula in Fig. S5.

Ox state	Coordination	Formula	Ni-O avg	Ni-O (4x)	Ni-O (2x)	Ref	Method
2.00	2	K_2NiO_2	1.690			[19]	XRD
2.00	4	Na_2NiO_2	1.895	1.90 (2x)	1.89 (2x)	[19]	XRD
2.00	4	Li_2NiO_2	1.900			[19]	XRD
2.00	4	$BaNiO_2$	2.000			[19]	XRD
2.00	6	La_2NiO_4	2.041	1.94	2.24	[20]	unknown
2.00	6	NiO	2.050			[21]	EXAFS
2.00	6	β-$Ni(OH)_2$	2.070			[22]	EXAFS
2.00	6	NiO	2.070			[14]	EXAFS
2.00	6	NiO	2.080			[23]	EXAFS
2.00	6	NiO	2.080			[22]	EXAFS
2.00	6	La_2NiO_4 (tetr.)	2.033	1.93	2.24	[19]	XRD
2.00	6	La_2NiO_4	2.037	1.93	2.24	[24]	XRD
2.00	6	La_2NiO_4 (orth.)	2.047	1.95	2.24	[19]	XRD
2.00	6	NiO	2.090			[19]	XRD
2.00	6	NiO	2.092			[23]	XRD
2.00	6	Average of $Ni^{II}O_6$	2.031 ± 0.038			This work	EXAFS & XRD
2.00	6	Average of $Ni^{II}O_6$	2.070 ± 0.011			This work	EXAFS
2.00	6	Calibration curve	2.070			This work	EXAFS
3.00	6	β-$HNiO_2$ (NiOOH)	1.923	1.87	2.03	[25]	EXAFS
3.00	6	$LaNiO_3$	1.940			[23]	EXAFS
3.00	6	NiOOH	1.950			[21]	EXAFS
3.00	6	$LiNiO_2$	1.970	1.92	2.07	[25]	EXAFS
3.00	6	$LaNiO_3$	1.918			[23]	XRD

Ox state	Coordination	Formula	Ni-O avg	Ni-O (4x)	Ni-O (2x)	Ref	Method
3.00	6	$LaNiO_3$	1.930			[19]	XRD
3.00	6	$NaNiO_2$	2.023	1.95	2.17	[25]	XRD
3.00	6	$NaNiO_2$	2.023	1.95	2.17	[19]	XRD
3.00	6	$LiNiO_2$	2.040			[19]	XRD
3.00	6	Average of $Ni^{III}O_6$	1.947 ± 0.046			This work	EXAFS & XRD
3.00	6	Average of $Ni^{III}O_6$	1.946 ± 0.020			This work	EXAFS
3.00	6	Calibration curve	1.944			This work	EXAFS
3.50	6	$H_{0.2}Na_{0.1}K_{0.2}Ni_{0.7}Co_{0.3}O_2$ * 0.5 H_2O	1.890			[25]	EXAFS
3.67	6	$K(NiO_2)O_3$	1.860			[21]	EXAFS
4.00	6	$NaNiIO_6$	1.863			[26]	EXAFS
4.00	6	NH_4NiIO_6	1.867			[26]	EXAFS
4.00	6	$RbNiIO_6$	1.869			[26]	EXAFS
4.00	6	$KNiIO_6$	1.870			[14]	EXAFS
4.00	6	$KNiIO_6$	1.873			[26]	EXAFS
4.00	6	$CsNiIO_6$	1.875			[26]	EXAFS
4.00	6	$BaNiO_3$	1.900	1.74	2.06	[19]	XRD
4.00	6	$KNiIO_6$	2.000			[27]	XRD
4.00	6	Average of $Ni^{IV}O_6$	1.890 ± 0.033			This work	EXAFS & XRD
4.00	6	Average of $Ni^{IV}O_6$	1.870 ± 0.003			This work	EXAFS
4.00	6	Calibration Curve	1.859			This work	EXAFS
3.76	6	B_i-NiCat	1.880			This work	EXAFS
3.34	?	KP_i-NiCat, A*	1.915			This work	EXAFS
3.26	6	KP_i-NiCat, B*	1.922			This work	EXAFS

If long and short distances are individually resolved, “Ni-O avg” gives the average weighted by the coordination number. This should be comparable to EXAFS measurements in which the individual distances are not resolved.

Table S3. Continued.

* The EXAFS spectrum of the KP_i-NiCat sample is of relatively low quality at high *k*-values, see Fig. S3. A and B denote two different simulation approaches. In A, the Debye-Waller parameter of the Ni-O interaction was taken from the B_i measurement. The data quality is not good enough to obtain a reasonable estimation of the coordination number (which is proportional to the amplitude of *k*-space oscillations). In B, additionally the coordination number was fixed to 6. However, the data quality is sufficient to estimate the Ni-O distances of the NiCat sample prepared in KP_i (*i.e.* zero-crossings of *k*-space oscillation are sufficiently resolved).

Estimation of the Ni oxidation state from the bond length (Fig. S5)

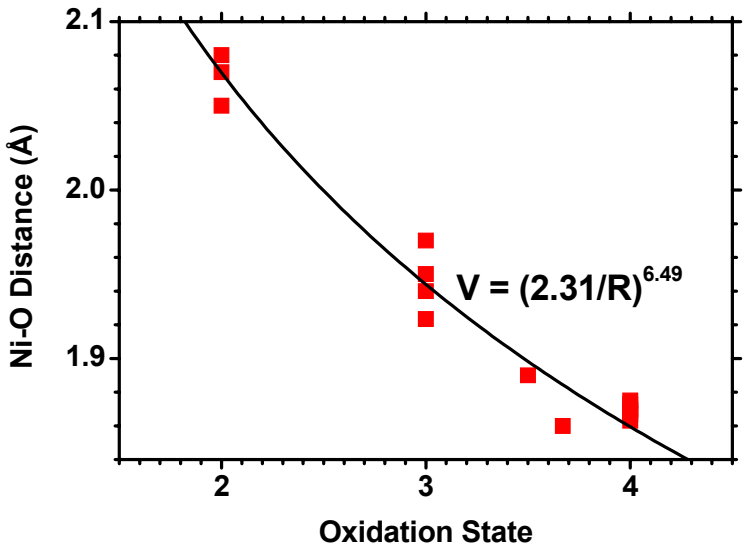

Figure S5. Calibration curve used for the estimation of the Ni oxidation state from the Ni-O bond length. Only the average EXAFS bond length (red squares) from Table S3 was used in the calibration. The black curve was obtained by fitting $y = (a/x)^b$ to the experimental data, using the option "non-linear curve fit" in Origin 8.0. We also tested a linear fit to the data and found that the differences in the oxidation-state estimates for the NiCat were small (±0.1 oxidation state; not shown).

References

1. Schaefers, F., M. Mertin, and M. Gorgoi, *KMC-1: A high resolution and high flux soft X-ray beamline at BESSY.* Review of Scientific Instruments, 2007. **78**(12): p. 123102.
2. Penner-Hahn, J.E., *X-ray absorption spectroscopy in coordination chemistry.* Coordination Chemistry Reviews, 1999. **190-192**: p. 1101-1123.
3. Bearden, J.A. and A.F. Burr, *Reevaluation of X-Ray Atomic Energy Levels.* Reviews of Modern Physics, 1967. **39**(1): p. 125-142.
4. Risch, M., F. Ringleb, V. Khare, P. Chernev, I. Zaharieva, and H. Dau, *Characterisation of a water-oxidizing Co-film by XAFS.* Journal of Physics: Conference Series, 2009. **190**: p. 012167.
5. Risch, M., V. Khare, I. Zaharieva, L. Gerencser, P. Chernev, and H. Dau, *Cobalt-Oxo Core of a Water-Oxidizing Catalyst Film.* Journal of the American Chemical Society, 2009. **131**(20): p. 6936-6937.
6. Dittmer, J., *Linear-Dichroismus-Röntgenabsorptionsspektroskopie zum katalytischen Zyklus des wasserspaltenden Mangankomplexes der Photosynthese in Theorie und Experiment*, in *Mathematisch-Naturwissenschaftliche Fakultät*. 1999, Christian-Albrechts-Universität: Kiel, Germany.
7. Rehr, J.J. and R.C. Albers, *Theoretical approaches to X-ray absorption fine structure.* Reviews of Modern Physics, 2000. **72**(3): p. 621-654.
8. Ankudinov, A.L., B. Ravel, J.J. Rehr, and S.D. Conradson, *Real-space multiple-scattering calculation and interpretation of x-ray-absorption near-edge structure.* Physical Review B: Condensed Matter, 1998. **58**(12): p. 7565-7576.
9. Rehr, J.J., J.J. Kas, M.P. Prange, A.P. Sorini, Y. Takimoto, and F. Vila, *Ab initio theory and calculations of X-ray spectra.* Comptes Rendus Physique, 2009. **10**(6): p. 548-559.
10. Dau, H., C. Limberg, T. Reier, M. Risch, S. Roggan, and P. Strasser, *The mechanism of water oxidation: from electrolysis via homogeneous to biological catalysis.* ChemCatChem, 2010. **2**(7): p. 724-761.
11. Ravel, B. and M. Newville, *ATHENA, ARTEMIS, HEPHAESTUS: data analysis for X-ray absorption spectroscopy using IFEFFIT.* Journal of Synchrotron Radiation, 2005. **12**(4): p. 537-541.
12. Stern, E.A., *Number of relevant independent points in x-ray-absrption fine-structure spectra.* Physical Review B, 1993. **48**(13): p. 9825-9827.
13. Eadie, W.T., D. Drijard, F.E. James, M. Roos, and B. Sadoulet, *Statistical methods in experimental physics*. 2nd ed. 1971, Amsterdam: North Holland.
14. Farley, N.R.S., S.J. Gurman, and A.R. Hillman, *Dynamic EXAFS study of discharging nickel hydroxide electrode with non-integer Ni valency.* Electrochimica Acta, 2001. **46**(20-21): p. 3119-3127.
15. Crespin, M., P. Levitz, and L. Gatineau, *Reduced forms of $LaNiO_3$ perovskite. Part 1.-Evidence for new phases: $La_2Ni_2O_5$ and $LaNiO_2$.* Journal of the Chemical Society, Faraday Transactions 2: Molecular and Chemical Physics, 1983. **79**(8): p. 1181-1194.
16. Dittmer, J., L. Iuzzolino, W. Dörner, H.-F. Nolting, W. Meyer-Klaucke, and H. Dau, *A new method for determination of the edge position of X-ray absorption spectra*, in *Photosynthesis: Mechanisms and Effects*, G. Garab, Editor. 1998, Kluwer Academic Publishers: Dortrecht. p. 1339-1342.
17. Dau, H., P. Liebisch, and M. Haumann, *X-ray absorption spectroscopy to analyze nuclear geometry and electronic structure of biological metal centers—potential and questions examined with special focus on the tetra-nuclear manganese complex of oxygenic photosynthesis.* Analytical and Bioanalytical Chemistry, 2003. **376**(5): p. 562-583.
18. Zaharieva, I., M.M. Najafpour, M. Wiechert, M. Haumann, P. Kurz, and H. Dau, *Synthetic manganese-calcium oxides mimic the water-oxidizing complex of photosynthesis functionally and structurally.* Energy Environ. Sci., 2011. **4**(7): p. 2400-2408.
19. Evarestov, R.A., V.A. Veryazov, I.I. Tupitsyn, and V.V. Afanasiev, *The electronic structure of crystalline nickel oxides.* Journal of Electron Spectroscopy and Related Phenomena, 1994. **68**: p. 555-563.
20. Medarde, M., A. Fontaine, J.L. Garcia-Munoz, J. Rodriguez-Carvajal, M. de Santis, M. Sacchi, G. Rossi, and P. Lacorre, *$RNiO_3$ perovskites (R=Pr,Nd): Nickel valence and the metal-insulator transition investigated by X-ray-absorption spectroscopy.* Physical Review B, 1992. **46**(23): p. 14975-14984.

21. Capehart, T.W., D.A. Corrigan, R.S. Conell, K.I. Pandya, and R.W. Hoffman, *In situ extended X-ray absorption fine structure spectroscopy of thin-film nickel hydroxide electrodes.* Applied Physics Letters, 1991. **58**(8): p. 865-867.
22. Pandya, K.I., W.E. O'Grady, D.A. Corrigan, J. McBreen, and R.W. Hoffman, *Extended X-ray absorption fine structure investigations of nickel hydroxides.* The Journal of Physical Chemistry, 1990. **94**(1): p. 21-26.
23. Levitz, P., M. Crespin, and L. Gatineau, *Reduced forms of $LaNiO_3$ perovskite. Part 2.-X-ray structure of $LaNiO_2$ and extended X-ray absorption fine structure study: local environment of monovalent nickel.* Journal of the Chemical Society, Faraday Transactions 2: Molecular and Chemical Physics, 1983. **79**(8): p. 1195-1203.
24. Müller-Buschbaum, H. and U. Lehmann, *Zum Problem der Oktaederstreckung an La_2CuO_4, La_2NiO_4 mit einem Beitrag über $CaSmAlO_4$.* Zeitschrift für anorganische und allgemeine Chemie, 1978. **447**(1): p. 47-52.
25. Demourgues, A., L. Gautier, A.V. Chadwick, and C. Delmas, *EXAFS study of the Jahn-Teller distortion in layered nickel oxyhydroxide.* Nuclear Instruments and Methods in Physics Research Section B: Beam Interactions with Materials and Atoms, 1997. **133**(1-4): p. 39-44.
26. Currie, D.B., W. Levason, R.D. Oldroyd, and M.T. Weller, *Synthesis, spectroscopic and structural studies of alkali metal-nickel periodates $MNiIO_6$(M = Na, K, Rb, Cs or NH_4).* Journal of the Chemical Society, Dalton Transactions, 1994(9): p. 1483-1487.
27. Vannerberg, N.G. and I. Blockham, *Crystal structure of potassium nickel(IV) hexaoxidoiodate(VII).* Acta Chemica Scandinavica, 1965. **19**(4): p. 875-878.